

Digital multishaping for white noise reduction and its implementation on programmable logic

Authors: Regadío , Dr. Alberto, G. Tejedor, Dr. J. Ignacio, Juan, Dr. J. Blanco, Sánchez-Prieto, S, Esteban, Dr. Luis, Regadío , Dr. Alberto

Date: 2026-02-04T21:38:13+00:00

Abstract

One of the most common noise types in particle physics detectors is white noise. Its impact inversely correlates with the shaping time of the signal. Extending the shaping time would significantly improve resolution in pulse height measurements, but it also increases the risks associated with pile-up and detector saturation, particularly at high particle arrival rates. A compromise on the shaping time is therefore required to balance these opposing effects. The originality of this study is to process pulses from a single particle detector with multiple shapers in parallel, enabling independent pulse analysis for each shaper. A Finite State Machine (FSM) then selects the optimal pulse height based on the current pulse arrival rate. The proposed method was implemented and evaluated using both Python and programmable logic. The results show that this technique is effective at reducing noise, as demonstrated through the analysis of energy histograms. Overall, this strategy offers a promising approach to enhancing particle detector performance, especially under fluctuating particle arrival rates.

Full Text

Preamble

Digital multishaping for white noise reduction and its implementation on programmable logic* Alberto Regadío,¹ † J. Ignacio García Tejedor,¹ Juan José Blanco,¹ Sebastián Sánchez-Prieto,¹ and Luis Esteban² ¹Space Research Group, Universidad de Alcalá, 28805 Alcalá de Henares, Spain ²Department of Electrical and Computer Engineering, University of Puerto Rico-Mayagüez, Mayagüez, Puerto Rico, USA One of the most common noise types in particle physics detectors is white noise. Its impact inversely correlates with the shaping time of the signal. Extending the shaping time would significantly improve resolution in pulse height measurements, but it also increases the risks associated with

pile-up and detector saturation, particularly at high particle arrival rates. A compromise on the shaping time is therefore required to balance these opposing effects. The originality of this study is to process pulses from a single particle detector with multiple shapers in parallel, enabling independent pulse analysis for each shaper. A Finite State Machine (FSM) then selects the optimal pulse height based on the current pulse arrival rate. The proposed method was implemented and evaluated using both Python and programmable logic. The results show that this technique is effective at reducing noise, as demonstrated through the analysis of energy histograms. Overall, this strategy offers a promising approach to enhancing particle detector performance, especially under fluctuating particle arrival rates.

Keywords: Digital filters, Digital shapers, Noise mitigation, Pile-up, Pulse height

INTRODUCTION

In particle spectroscopy, detector chains determine the energy of incoming particles while coping with noise. In this context, the shaping stage is a fundamental component.

Digital electronics have largely replaced analog implementations in particle-detection chains, driven by the development of integrated circuits and their advantages (e.g., multistage integration in a single device, reduced volume, and reconfigurability). Digital pulse shaping pursues the same goal as analog shaping, namely filtering the signal to enhance system resolution. Its versatility enables the implementation of pulse shapes such as triangular, trapezoidal, cusp-like, or flat-topped cusp-like shaping [1], which can be more challenging to realize with analog electronics.

Despite the rise of neural networks and artificial intelligence in this field [2], both analog and digital filters have the fundamental advantage of being linear and easy to implement in both hardware and software. When considering digital shaping as a filtering process, two fundamental implementations of digital shapers must be considered: Infinite-Impulse Response (IIR) filters and Finite-Impulse Response (FIR) filters [3, 4]. The types of noise mitigated by both can be effectively analyzed in the frequency domain. However, in particle detection, it is also common to analyze them in the time domain [5-8]. Although there are generalizations [9, 10], three noise components: white noise, $1/f^2$ -noise (also called Brownian), and $1/f$ -noise are usually dominant in a signal processing chain for acquisition of the signals from capacitive sources. * Supported by the project SBPLY/21/180501/000170, cofunded by the Junta de Comunidades de Castilla-La Mancha and by the European Regional Development Fund, FEDER. Supported by the project PID2022-140218NB-I00, funded by Ministerio de Ciencia e Innovación (Spain Government). † Corresponding author, alberto.regadio@uah.es The effect of these noise types in a detection chain can be modeled using the Equivalent Noise Charge (ENC) formula pre-

sented in [7, 8, 11]: $n f C_i$ where Q_n is the ENC in Coulombs, i_n is the current noise Hz, e_n and e_{nf} are the volt- spectral density measured in A/ age noise and $1/f$ -noise spectral density measured in V/ and C_i is the equivalent detector capacitance (in Farads). $F^2 n f$ are the noise indexes, that is the impact of a specific type of noise according to definition given by [5], for white noise (in units of $1/s$), $1/f^2$ -noise (in s), and $1/f$ noise (dimensionless), respectively. This formula is applicable to both analog and digital shapers. i , and F^2 The influence of $1/f$ -noise remains independent of the shaping time. The impact of $1/f^2$ -noise $F^2 i$, characterized by its $1/f^2$ noise spectrum, is proportional to the shaping time.

Throughout this article, we will focus mainly on symmetric shapers, namely triangular, as they offer a good Signal- to-Noise Ratio (SNR) against white noise and because they are easily implementable with digital circuits. In particular, in the case of a specific type of symmetric shapers, namely trapezoidal or triangular (Fig. 1 [Figure 1: see original paper]) it is straightforward that the impact of this noise type is where $F^2 i$ is the noise index of the $1/f^2$ -noise, τ_p is the duration of the plateau of the trapezoid, and τ_r is the rising time of the shaped signal. Notice that in case that the detection chain is dominated by $1/f^2$ -noise, the solution is straightforward: pulse shaping with very short shaping times whenever the ballistic deficit allows it and we are interested in losing as few pulses as possible.

In contrast to $1/f^2$ -noise, white noise tends to have an inverse relationship with shaping time, suggesting that longer rates. This method ensures accurate dead time corrections and high-resolution energy spectra.

A pile-up correction method is introduced in [26] using several shapers for pulse reconstruction and subsequent Pulse Height Analysis (PHA). In [27], instead of employing different shapers, specific pulse shapes generated by α and β particles are used to precisely measure pulse heights.

A real-time algorithmic pile-up correction on pulses of known shape using diverse modules in the detection chain is presented in [28].

In [25], energy recovery for individual pulses in pile-up events is also achieved with algorithms.

Both methods achieve good resolution with a small number of rejected pulses.

Pile-up correction has also been tackled using evolutionary algorithms [29] and deep-learning [30, 31]. With respect to the latter, although highly effective, they rely on nonlinear processing and require prior training and a certain level of computing.

The objective of this method is not to rely on a single detector chain, but rather to utilize multiple detection chains concurrently, further minimizing pile-up and saturation effects.

An implementation of a similar method was performed in [32], although in this

case the shaping is digital and at the end we add additional electronics for pulse selection as we will see later.

Each chain employs its own shaper, facilitating independent measurement of pulse height and allowing for the selection of the most suitable shaping based on the pulse arrival rate. One advantage of the method outlined in this article is its flexibility: the employed shapers can be changed without needing a redesign of the rest of the circuit elements. This versatility also lends itself to ease of implementation in digital logic. The approach aims to optimize noise influence within the detection chain, particularly in scenarios dominated by white noise.

Fig. 2 [Figure 2: see original paper] illustrates an example of the optimal shaping time τ^* . In this context, pile-up and saturation effects broaden the noise spectrum, i.e. increase the ENC, represented in this Figure as additional serial white noise. When this happens, it is necessary to adjust the shaping time to τ^\dagger to mitigate these effects, minimize the ENC, and enhance resolution.

The rest of the paper is organized as follows: In Section II the proposed method is explained. An analysis of this method within its expected efficiency is exposed in Section III. The results are presented in Section IV and V and its implementation in reconfigurable logic is described in Section VI. Finally, Section VII summarizes the conclusions of this work.

II. METHOD To implement this method, we start with the conventional approach of employing a single detection chain, that is with a shaping stage preceding the PHA stage. For this setup, M parallel detection chains are used and the pulse height analysis is determined by a FSM. Their shapers ($0, \dots, M - 1$) are FIR and time-invariant and have the particularity that they provide the same pulse shape but with shaping times Fig. 1. Time parameters of trapezoidal shaping: rising, plateau and falling time (τ_r , τ_p , and τ_f , respectively). The sum of these three is the shaping time τ . Hereafter only symmetrical shapings will be considered and therefore $\tau_r = \tau_f$. Shaping times could effectively reduce errors in pulse height measurements. Namely, for trapezoidal or triangular shaping its impact ([5], among others) is where F_{2v} is the white noise index.

According to these formulas, there exists an optimal shaping time τ^* that minimizes the ENC. There are algorithms available to optimize pulse shaping with the objective of minimizing noise, including analytical methods (e.g., [9, 12-14]), neural network-based approaches (e.g., [15]), and genetic algorithms (e.g., [16]), among others. Nonetheless, in certain situations, the search for τ^* is difficult.

In addition, many detectors experience fluctuations in particle arrival rates over time, making this optimization more difficult. Consequently, the optimal shaping time becomes a dynamic parameter, requiring careful consideration and adjustment to maintain optimal performance.

Without pretending to be exhaustive, while $1/f^2$ noise remains significant in

many detectors due to thermal agitation of charge carriers—particularly in semiconductor-based detectors—and $1/f$ noise can arise from fluctuations in the electron multiplication process, the main source of white noise is typically the preamplifier electronics [17]. The impact of this white noise is magnified when the event arrival rate is very high, requiring a low shaping time to prevent pile-up and saturation. For the purposes of this manuscript, we will assume that serial noise is the dominant noise factor.

Note that a short shaping time does not necessarily cause a ballistic deficit as long as it is high enough to avoid this problem [18].

Pulse processing has been developed for particle detectors to enhance resolution and mitigate pile-up effects at the same time [4]. In addition to classical methods for avoiding pile-up (e.g. [19]), another common approach involves reducing convolution time through windowing [20] and unfolding (i.e. deconvolution) [21–24], including some variations [25], albeit at the expense of increasing white noise. Many of these approaches are implementable in digital electronics. However, the cited works do not employ more than one shaper working in parallel.

In [14], a multi-parametric analysis is conducted using delay-line based shapers to determine pulse heights, enabling high-performance particle energy measurements even at high τ_{eff}

3 Fig. 2. (Color online) At high particle arrival rates, pile-up and saturation effects cause the ENC2 curve to shift to ENC1, resulting in an increase in noise levels. In such cases, our objective is to adjust the shaping time, as indicated by the red arrow, to reduce noise levels.

This adjustment helps mitigate the impact of pile-up and saturation effects, thereby improving the overall performance of the system.

Pile-up and saturation, which can be modeled as temporally correlated noises, were plotted as $1/f^2$ noise although the exponent value could change as long as it is greater than 1. $\tau_{\text{eff}} < \tau_{\text{M}} - 1$ such that $0 < \tau_{\text{eff}} < \tau_{\text{M}} - 1$.

Fig. 3 [Figure 3: see original paper]. (Color online) Proposed scheme of implementation of the presented method, where $x(t)$ is the signal at the output of the preamplifier and $y[n]$ is the pulse height.

In this article, $M = 3$ as depicted in Fig. 3. While reducing the number of detection chains to $M = 2$ may lead to a decrease in the efficiency of this method, increasing M would require additional hardware resources and complicate the FSM. Triangular shapers (i.e. $\tau_{\text{p}} = 0$ in Fig. 1) were chosen for their simple implementation as FIR filters in digital electronics, and because a long plateau time increases the $1/f^2$ -noise according to Eq. (2); however, other shapers could be chosen. An exhaustive comparison between combinations of shapers is beyond the scope of this paper. Fig. 4 [Figure 4: see original paper] shows pulses with different noise levels filtered by the shapers.

In this figure and in the following ones, all pulse weights are normalized, being

1.0 the saturation level.

The PHA stage comes after the shaping stage. In this study, only pulses with heights above a certain threshold (0.1) are detected, and the detection of the next pulse height cannot occur until the signal falls back below this threshold. The Fig. 4. (Color online) Example of pulses with different white noise power levels (PN) added, after the three parallel shaping stages.

Shaping time: $t_0 = 10$ ms (in blue), $t_1 = 20$ ms (in red), and $t_2 = 40$ ms (in green). In all the panels, $f = 10$ events/s. threshold can be adjusted based on the noise conditions of the detection chain. While more advanced versions of PHA exist [33], using a dynamic threshold level, the aim of keeping the PHA stage as simple as possible is to emphasize the effect of shapers on pulse height measurements.

The method with $M = 3$ operates as follows: the pulse heights obtained from the three detection chains (C0, C1, and C2) are fed into the FSM of Fig. 5 [Figure 5: see original paper]. The FSM comprises five states (S0, S1, S2, S3 and S4), being the former the initial state. If C0 detects a pulse, the FSM moves to state S1 and a counter denoted by t starts. In this state, three situations are contemplated:

1. Another pulse from C0 may arrive quickly ($t < t_1 - t_0$). In this case, the S1 state is kept and the previous pulse from C0 is put at the output $y[n]$ (denoted as 0-).

This is a typical case with high pulse rates.

2. Another pulse may arrive from C1. This pulse is supposed to be the previous one of C0 and there is a transition to S2.

3. No pulses are detected from C0 nor C1. In this case, when $t > t_1 - t_0$ the system is reset returning to S0 and put at $y[n]$ the last pulse detected by C0.

In S2, two situations are contemplated:

1. Another pulse in C0 is detected. In this case, the pulse stored in the 2nd case of the previous list is put at the output $y[n]$ and the FSM returns to S1 to see if more pulses are coming.

2. A certain minimum separation time ($t > t_0$) may elapse. In that case, the FSM goes to S3, because if Equivalent noise charge [10 C] 10050201015210.10010110.0Shaping time s]-17 noisennoise1/f noiseENC

1pile-up andsaturationeffectsgapENC $2\tau\uparrow\tau^*$ [μ whitebrownianFSM OutputPulse
 HeightAnalysisDigitalshaper 1Pulse HeightAnalysisADCDigitalshaper 2Pulse
 HeightAnalysisProgrammableLogicData Acquisition Boardy[n]x(t)Digitalshaper
 0y [n]1y [n]2y [n]3x[n]0.000.250.500.751.00amplitude [a.u.]PN=0.025 103PN=0.100
 1030200400time [ms]0.000.250.500.751.00amplitude [a.u.]PN=0.400 1030200400time
 [ms]PN=2.500 103

4 To perform a proof of concept and evaluate the results, the algorithm was first coded in Python using the Numpy library [34]3.

An example of output is shown in Fig. 6 [Figure 6: see original paper], where the input signal $x[n]$ and the output signal $y[n]$ are observed. We can see that when there is no overlap, the sequence S0, S1, S2 is produced, and the pulse captured by the chain that offers less noise is returned.

The objective is to adapt to the varying frequencies of pulse arrivals without losing any of them. When the arrival rate is very low, the detection chain that effectively filters the noise, typically C2, is prioritized due to its high τ compared to the others. In contrast, when pile-up and/or saturation occurs, the chains that return the pulses are C1 or C0. This minimizes the loss of pulses due to a low τ by the shaper while improving the resolution of the detection chain, similar to one with a shaper featuring a high τ .

All of this is achieved by configuring each digital shaper, replicating the PHA, and implementing the described FSM.

Note that this method assumes that the arrival time of each detected event can be delayed within an interval between 0 and $\tau M - 1 - \epsilon$. While this does not pose a significant issue for creating histograms, it may impact measurements that rely on precise timing, such as Time Of Flight (TOF) and (anti) coincidence measurements. Nevertheless, this effect can be corrected if we know which detection output $y_i[n]$ is selected at the output $y[n]$ to return the pulse height.

III. EFFICIENCY OF THIS METHOD As stated in Section I, the main objective of this method is reducing the noise index F_{2v} . With this goal in mind, we define P_k as the probability that the detection chain k is the one that performs the PHA of the event.

The value of P_k is calculated when given an event, what is the probability that in a given interval the next event will occur again. If that interval is within the shaping time, a pile-up will happen. P_k can be modeled as a Poisson distribution.

According to it, according to it, for an average rate of arrival of f events per second, the probability of an event occurring in a time interval $[\tau_k, \tau_{k+1}]$ is $P_k = p(\tau_k < t \leq \tau_{k+1}) = p(t \leq \tau_{k+1}) - p(t \leq \tau_k) = (1 - e^{-f\tau_{k+1}}) - (1 - e^{-f\tau_k})$ Given M detection chains ordered by the shaping time, where 0 is the one with the minimum τ and $M - 1$ the one with the maximum τ , the probability of no pile-up for all detection chains is $P_{M-1} = p(\tau_{M-1} < t \leq \infty) = 1 - (1 - e^{-f\tau_{M-1}})$ Fig. 5. FSM proposed for 3 shapers. Each

transitions is denoted with two elements separated by a bar; the former is the trigger condition (C0, C1 or C2); the latter, the output at $y[n]$ (0, 1, 2). a new C0 arrives, it will already be sufficiently separated for either history to repeat itself or for the pulse to be detected by the rest of the chains. In this way, we guarantee that if we move to S3, a minimum amount of time will have passed since the previous C0, and therefore it will be a pulse candidate to be detected in C1.

In S3, three situations are considered:

1. Another pulse from C0 may arrive quickly. In this case, the systems returns to S1 and the previous pulse from C1 is put at the output $y[n]$.

2. Another pulse may arrive from C2. This pulse is supposed to be the previous one of C0 and C1 and there is a transition to S3.

3. No pulses come from C0 nor C2. In this case, when $t > \tau_2 - \tau_1 - \tau_0$ the system is reset returning to S0 and put at the output the last pulse of S1.

Finally, in S4 where again two things can happen:

1. A new pulse from S0 arrives, in which case we put the last pulse from S1 at the output and return to S1.

3 The Python and VHDL code used for this method is available at

therefore it is put at $y[n]$. <https://github.com/arc140181/multishaping>.

S0S1S2S3C0/-C1/-0/-S4C2/-0/2C0/0-C0/0-C0/1C0/110/0210/1—

5 Fig. 6. (Color online) Example of chronogram with $N = 0.01$ and $f = 15$ events/s for each signal enumerated in Section II.

In this case, the shaper that carries out the shaping is $M -$

1. Similarly, if $p(\tau M - 1 < t \leq \tau M - 2)$ then the shaping is performed by $M - 2$ and so on until the shaper of the first detection chain C0. The probability that two events are so close to each other that even the shaper or C0 can not avoid the pile-up, defined as P_{-1} is $P_{-1} = P(0 < t \leq \tau_0) = 1 - e^{-f \tau_0}$ that stands for Therefore, we can calculate a new term F^* the new effective white noise index, replacing $F^2 v$. This new term is equal

to the weighted mean that the detection chain v_k defined as the value of F_{2k} calculates the pulse height F_{2k} for the shaper k . This weighting mean is calculated with the probability P_k in this way: $1 - P_{k-1}$ (cid:88) $P_k F_{2k}$. The term prior to the summation is the inverse of the probability that the pulse height can be calculated with no pile-up and can be considered as the partition function. As said before, this equation replaces $F_{2k} v_k$; which for trapezoidal and triangular shapers in particular, was shown in Eq. (3). The particular value for trapezoidal and triangular shapers was shown in Eq. (3).

With this equation, given τ_k , the main objective is to mini-

2. For this, the following formula can be used

imize $F^* = 0$, $k \in \{0, \dots, M-1\}$ and then solve the system of equations. Our experience tells us that if $M > 2$, the system is complicated to solve or approximate analytically and other methods should be employed.

To optimize Eq. (7) as a function of τ_k as shown in Eq. (8), the gradient descent algorithm was programmed in Python using the Tensorflow package [35]. For this purpose, a fixed value of τ_k was established before running the optimization, which is also a factor that determines the number of pulses that one is willing to lose according to (6). The results for the new noise index are shown in Fig. 7 [Figure 7: see original paper]. For clarity in the results shown, optimizations were carried out for $M = 1, 2, 3, 4$.

The case of $M = 1$ (a single-shaper classic detection chain) was also calculated for comparison purposes. This particular case does not require optimization, it is sufficient to use (3). The first thing that can be inferred in Fig. 7 is that F^* creases as we are willing to lose pulses. Reductions of around 65% are also observed when we switch to using 2 chains instead of 1. These reductions continue to occur, although to a lesser extent as we increase M beyond 4. Notice that these Fig. 8 [Figure 8: see original paper]. (Color online) Graphical representation of the optimum shaping time for M shapers, for $f = 10$ events/s. The percentage of pulses lost is expressed on a per unit basis. noise spectrum, resulting in a typical deviation σ of the measurement. Noise was then added to the signal using a random normal distribution with a standard deviation σ , so the noise power PN is σ^2 . Observe that PN is directly proportional to e^{-2n} in Eq. (1). The σ value is directly proportional to the Full Width at Half Maximum (FWHM); specifically, $FWHM = 2.35 \cdot \sigma$ [17]. Also, remember that the ENC presented in (1) and denoted by Q_n and FWHM are, in turn, also directly proportional to each other [17]. Therefore, disregarding all non-white noise types, σ is also proportional to F_v .

For this test, a maximum pulse loss of 9.5% was chosen, and in simulations, we set $f = 10$ events/s. Therefore, according to (6), this constraint yields $\tau_k = 10$ ms. With this initial value, the optimal shaping times to minimize the equivalent white noise are those shown in Table 1. Note that even using a shaper with this characteristics, additional pulses could be recovered with an

additional processing stage, such as the method described in [19], but in this work, we will consider them lost.

In the histograms shown in Fig. 9 [Figure 9: see original paper], the variance difference becomes evident as white noise is increased. Notably, with the detection chain whose shaper is C0, the width of the histogram, represented by σ , is the highest. Furthermore, it is apparent that the detection chain of C2 exhibits a low σ but 2 depending of the percentage of Fig. 7. (Color online) Value of $F * \text{pulses lost}$ (x-axis), which is conditioned by $\$0$ for $M = 1, 2, 3, 4$. 2 are the theoretical minimums for white noise values of $F *$ and that other factors such as saturation voltage, which for the sake of clarity was not modeled in this section, can increase As already explained, the optimization of (7), fixing $\$0$, also yields the optimal value of the shaping times. These values are shown in Fig. 8 for $M = 2, 3, 4$. Note that in all three cases, if one is willing to lose more pulses (by increasing $\$0$), *theshapingtimeoftheothershapers* ($\$1, \dots, \tau M - 1$) is lengthened to produce the results shown in Fig. 7. Remember that the values shown in the last two figures are for white noise and for a triangular shaping. If the parallel white noise had been considered, there would be another equivalent par- 2, which would be calculated in the same allel white noise $F *$ way as in (7) and would cause an increase in the values of the noise index in Fig. 7 for high shaping times yielding curves similar to those in Fig. 2.

In the following Section we will test these formulas for the particular case $M = 3$ using all the elements of a real detection chain.

IV. SIMULATION RESULTS To validate the performance of the presented method, a series of simulations and tests were performed. The results presented in this study were also obtained using Python, employing the same packages listed in Section II for ease of handling the results. It is important to note that both the Python and VHDL implementations exhibit the same behavior. This ensures the consistency and reliability of the findings across different implementation platforms.

In this test, synthetic pulses with a height $h = 0.5$ were generated with an arrival rate f measured in events per second over a duration of 2000 seconds. This height was set because is the intermediate value between 0 (no signal) and 1 (saturation), and because in the absence of noise and pile-up, the histogram should exhibit a delta centered at 0.5. However, the presence of noise and pile-up will inevitably broaden the $*0.0200.0680.1130.1560.1970.237\text{percentageofpulseslost}M = 3$ 0 1 20.0000.0250.0500.0750.1000.125*shapingtime*[s]0.0200.0680.1130.1560.1970.237*percentageofpulseslost*M 4 0 1 2 $\$3$

Table 1. Pulse characteristics at the output of the three triangular shapers selected for this section. With these values, and in agreement with (7), $F * 2 = 0.136$.

Shaper Prob. of capture (4) 10 ms 0.400 $P0/(1 - P-1) = 11.2 \%$ 22 ms 0.182 $P1/(1 - P-1) = 29.3 \%$ 62 ms 0.065 $P2/(1 - P-1) = 60.5 \%$ fails to capture

all the pulses that have occurred. Additionally, when employing the proposed method (Multishaper), it is observed that σ resembles that of the detection chain of C2 but the system manages to capture more pulses. Finally, notice that the percentage of contribution of each shaper is practically the same as that in Table 1.

Fig. 10 [Figure 10: see original paper]. (Color online) Histograms generated varying the event rate.

The percentage of contribution of each shaper $y_0[n]$ (blue), $y_1[n]$ (red), and $y_2[n]$ (green) to the output $y[n]$ is shown at the left of each histogram.

Fig. 9. (Color online) Histograms generated varying noise. The percentage of contribution of each shaper $y_0[n]$ (blue), $y_1[n]$ (red), and $y_2[n]$ (green) to the output $y[n]$ is shown at the left of each histogram.

We also have computed histograms again during 2000 s to examine the influence of arrival rate due to pile-up effects. In this context, the rate f is defined as the mean number of input pulses per second.

When noise is limited but the pulse frequency increases, it becomes evident that not all pulses are captured by the shapers with a higher shaping time, resulting in count losses, as depicted in Fig. 10.

When testing a combination of noise values with arrival rates, we observe that the pulse widths have the behavior shown in Fig. 11 [Figure 11: see original paper]. Notice that when a high f is selected, pile-up and saturation effects are very common, and the output is almost always the output of the detection chain whose shaper is C0 (bottom right panel of Fig. 9). For the same reason, when a low f is selected, the output is almost always the output of C2 reducing σ by approximately half for $PN = 0.1$.

Moreover, when testing a combination of noise values with frequencies, we observe that the percentage of captured pulses exhibits the behavior shown in Fig. 12 [Figure 12: see original paper]. We note that this shaper captures as many pulses as C0 does, i.e. a value Fig. 11. (Color online) Histogram of σ of the captured pulses depending of PN and f in events per second. close to 100%.

Fig. 12. (Color online) Histogram of the percentage of the captured pulses in function of PN and f in events per second.

In summary, the resolution notably improves with high pulse arrival rates. This involves employing multiple linear shapers with nonlinear processing (the FSM) applied at the end. Naturally, the extra captured pulses using this method may exhibit more noise, but they are at least captured.

When the arrival frequency of pulses remains constant, employing this method may not be necessary. Instead, a detection chain with an optimal shaping time is sufficient. However, this is not typically the case in most situations. The best results for this method are observed when the detector processes pulses with variable arrival rates.

In our approach, pulse capture has been simplified to its maximum extent. While more complex systems, such as those involving deep learning (e.g., [30, 36]), may yield better results, implementing them on reconfigurable devices poses 0.420.440.460.480.500.520.540.560.58010002000300040005000countsPN=0.025 103 f=10 ev/sS0. 91.84%=1.03102S1. 82.40%=0.21102S2. 57.09%=0.19102Multi. 86.42%=0.221020.420.440.460.480.500.520.540.560.58050010001500200025003000PN=0.100 103 f=10 ev/sS0. 91.89%=1.18102S1. 82.23%=0.43102S2. 56.80%=0.31102Multi. 86.36%=0.411020.420.440.460.480.500.520.540.560.58pulse height02004006008001000120014001600countsPN=0 103 f=10 ev/sS0. 91.55%=1.53102S1. 82.42%=0.85102S2. 57.22%=0.54102Multi. 85.91%=0.771020.420.440.460.480.500.520.540.560.58pulse height0100200300400500600PN=2.500 103 f=10 ev/sS0. 91.73%=3.26102S1. 82.37%=2.15102S2. 57.03%=1.42102Multi. 86.27%=1.9010211.7%35.2%53.0%12.2%35.1%52.7%11.8%34.7%53.6%12.3%34.7%53.0%0.4800.4850.4900.4950 103 f=5 ev/sS0. 95.25%=0.31102S1. 89.45%=0.21102S2. 72.89%=0.13102Multi. 89.30%=0.161020.4800.4850.4900.4950.5000.5050.5100.5150.52002004006008001000120014001600PN=0.025 103 f=10 ev/sS0. 91.98%=1.03102S1. 82.97%=0.21102S2. 56.93%=0.21102Multi. 86.36%=0.231020.4800.4850.4900.4950.5000.5050.5100.5150.520pulse height050010001500200025003000countsPN=0 103 f=50 ev/sS0. 66.12%=4.74102S1. 39.36%=1.86102S2. 7.61%=1.45102Multi. 63.50%=0.671020.4800.4850.4900.4950.5000.5050.5100.5150.520pulse height05001000150020002500PN=0.025 103 f=100 ev/sS0. 42.69%=10.26102S1. 15.03%=5.62102S2. 1.10%=5.23102Multi. 41.52%=5.351026.3%20.3%73.4%11.3%35.2%53.5%46.2%50.0%3.9%68.6%31.0%0.4%0.010.060.10.15N0.0010.0 00.010.060.10.15NShaper 10.010.060.10.15NShaper 20.010.060.10.15NMulti- shaping0.000.010.020.030.04PPPP0.010.060.10.15N0.0010.0150.0290.0420.0560.07fShaper 00.010.060.10.15NShaper 10.010.060.10.15NShaper 20.010.060.10.15NPPPMulti- shaping0%20%40%60%80%100%P

420 additional challenges unless implemented in software.

V. RESULTS IN MITO INSTRUMENT This section shows the algorithm described in this article working in a Muon Impact Tracer and Observer (MITO) instrument. Unlike in the simulation, where the improvement in resolution has already been demonstrated, in this section the pulse height spectrum has a different distribution. We will also see that the algorithm improves the results.

MITO is a directional muon telescope [37]. It is composed of only two stacked scintillators of 1 m² each, with eight Photo Multiplier Tubes (PMTs) gathering the light emerging from the four lateral sides of the scintillators. It also has an optional lead layer between the scintillator enclosures that allows the filtering of unwanted particles depending on the type of application. MITO has been conceived not only to achieve muon flux registering, but also to determine muon arrival directions through the capture and analysis of pulse height data from the multiple PMTs. Currently, this telescope model is working in Antarctica and the Izaña Observatory, (Tenerife Island, Spain). There is also another MITO work- ing in Turkey [38].

To determine the arrival direction, the impact point in both scintillators (Top and Bottom) is inferred from the pulse heights in the four PMTs associated to each. In short, and oversimplifying, the closer the particle has struck the scin- tillator from PMT, the higher the detected pulse will be. A more detailed

description of trajectory determination techniques can be found in [37, 39, 40].

Independently of the method used, an accurate pulse height measurement in each PMTs is necessary to measure the point of impact of muons and therefore their arrival direction. As mentioned in the previous section, a key value is the shaping time of the first detection chain t_0 . The lower it is, the fewer pulses will be lost, but the noise will also be greater, providing false pulses to the detection chain that could distort the arrival direction measurements. On the other hand, the higher the shaping time is, the less noise the pulse will contain, but more pulses will be lost because pulses can appear overlapped due to periods with a high muon arrival rate.

In order to adjust the shaper parameters to the rate of incoming pulses, we performed the proposed algorithm offline.

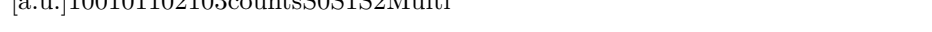
However, it could be run online in configurable logic (Section VI). For this, we processed each individual pulse from the photomultiplier with three triangular shapers S0, S1, and S2 (with shaping times of 20, 60, and 120 μs , respectively), as we did in the simulation. An example of an individual pulse arriving from one of the multipliers and processed by the three shapers and the PHA is shown in Fig. 13 [Figure 13: see original paper]. In this figure, we can see how, the noise becomes indeed more evident when the shaping time is shorter, thus affecting the pulse height.

When we generate a histogram with these heights and compare the results (Fig. 14 [Figure 14: see original paper]), we see that the technique presented adapts very well to S1 and S2 results, discarding the false pulses of S0 (see the part of the spectrum enclosed by the grey rectangle). An individual pulse processed by the 3 detection chains composed by shapers S0, S1, and S2 and the same pulse height analyzer. This is because when an isolated pulse appears in time only in the S0 chain, that pulse is discarded since it would also have to be detected in S1 and S2 according to Fig.

Fig. 14. (Color online) The spectrum of a PMT of MITO whose pulses have been processed by C0, C1, C2, and the proposed algorithm.

To test the behavior of the algorithm against pile-up, we generate a histogram with only overlapping pulses (Fig. 15 [Figure 15: see original paper]).

We observe that long shapings such as S1 or S2 do not detect all pulses, so the algorithm practically only stores the heights that the S0 detection chain detects.

In any case, if we return to the case where all the points in Fig. 14 are present, we see that using the technique described in this article improves the results when determining the PMT height spectrum by selecting the input from the three detection chains. 

9 (Color online) The spectrum of a PMT of MITO whose Fig. 15. pulses were processed by S0, S1, S2, and the proposed algorithm.

For these histograms, only overlapped pulses have been taken into account.

IMPLEMENTATION IN CONFIGURABLE LOGIC To test the proposed method in a real detection chain, the proposed scheme depicted in Fig. 3 has been implemented in a programmable Field Programmable Gate Array (FPGA) device. Instead of a complete system with several channels as in [41], in this section we will focus specifically on the module that implements the proposed algorithm.

For this project, tools from the Xilinx family were employed to synthesize the design in a Spartan-7 FPGA, specifically a XC7S75FGGA676-1 device. The implementation was executed using generic VHDL without relying on any specific component of the device. As a result, synthesizing this design in any other FPGA from a different manufacturer should not pose any issues.

The coding has been divided into (a) shaping, implemented as a FIR filter; (b) PHA according to the explanation in Section II; (c) FSM that yields the output pulse heights. Fig. 16 [Figure 16: see original paper] shows a general diagram of the connections between the shaper, PHA and FSM modules. As can be seen, it is similar to the one in Fig. 3.

All the interfaces have in common the resolution in bits W of the signals. Apart from signals CLK (clock signal) and RST (reset signal), which are common for all the proposed interfaces, in the case of the shaper, the input signals are: X: input signal from the Analog-to-Digital Converter (ADC); XEN: input signal enable. The output signals are: Y: shaped signal; YEN: shaped signal valid. The shaping type and duration are configured internally.

The input signals of the PHA are: X: input signal from shapers; XEN: input signal enable. The output signals are:

Y: pulse height (zero if no pulse detected); YEN: pulse height detected; LAST: height of the last pulse detected. The threshold level (see Section II) is a parameter of this component selected during synthesis.

Finally, the input signals of the FSM are: IN0, IN1, Fig. 16. Proposed scheme of implementation of the presented method in VHDL with its corresponding interfaces. CLK and RST connections and Shaper 1, Shaper 2, PHA 1 and PHA 2 are omitted for clarity.

Table 2 . Resources used in a Xilinx XC7S75FGGA676-1.

Resource	Slice LUTs (logic)	Slice registers	Bonded IOB	Clock buffers	Other resources
Number					
Percentage					
IN2:	pulse heights detected; IN0EN, IN1EN, IN2EN: pulse heights detected valid; LAST0, LAST1, LAST2: height of the last pulses detected by PHAs. The output signals are: Y: pulse height (zero if no pulse detected); YEN: pulse detected.				

Table 2 shows a table of the components used for $W = 14$ in a Xilinx XC7S75FGGA676-1. This FPGA has very limited resources within the Spartan-7 family. However, the proposed design fits perfectly. Note that

specific resources from this architecture or from Xilinx, such as Digital Signal Processing Instead, generic resources (DSP) modules, were not used. have been employed to make the design transferable to other programmable devices, even from manufacturers different to Xilinx. If an FPGA with more resources is used and specific resources are employed, it would be possible to replicate the proposed method for multiple detectors using a single device.

VII. SUMMARY The evaluation of pulses coming from particle detectors using several shapers at a time instead of one, and evaluating the results of all of them at a later stage, improves the resolution of the detection chain and maximizes the number of captured pulses. This improvement stems from the ability to adapt shaping times based on the particle arrival rate: longer shaping times mitigate white noise, while shorter shaping times help to avoid pile-up and saturation. Despite the fact that this scheme can be implemented for an arbitrary number of shapers, in this article we focused on using 3 shapers, which 02000400060008000pulse height [a.u.]100101102countsS0S1S2MultiRSTCLKYYENWXXENRSTCLKYYENWXXENLASTRSTCLKYY

OPHA 0FSM.....
551 represents a good tradeoff between performance and system complexity. Also, while adjusting the number of shapers may complicate the presented FSM, changing the shaping time is practically instantaneous, allowing the system to easily adapt to each specific situation. The FSM does not claim to be faultless, but rather to demonstrate that it is possible to work with more than one shaping chain at the same time in order to improve the resolution of the entire detection chain. Finally, we demonstrated that the approach is fully implementable in both software and configurable logic. [1] J. Liu, J. Yang, G.-Q. Zeng, K.-Q. Zhang, S.-L. Wei, and L.-Q.

Ge, Nuclear Science and Techniques 28, 1 (2017). [2] W.-B. He, Y.-G. Ma, L.-G. Pang, H.-C. Song, and K. Zhou, Nuclear Science and Techniques 34, 88 (2023). [3] V. T. Jordanov and G. F. Knoll, Nuclear Instruments and Methods in Physics Research Section A: Accelerators, Spectrometers, Detectors and Associated Equipment 345, 337 (1994). [4] J.-X. Li, H.-L. Hou, Y.-F. Huang, M.-S. Cheng, and Z.-M. Dai, Nuclear Science and Techniques 34, 165 (2023). [5] F. Goulding, Nuclear Instruments and Methods 100, 493 (1972). [6] F. S. Goulding and D. A. Landis, IEEE Transactions on Nuclear Science 29, 1125 (1982). [7] V. Radeka, "Signal processing for particle detectors," in Particle Physics Reference Library: Volume 2: Detectors for Particles and Radiation, edited by C. W. Fabjan and H. Schopper (Springer International Publishing, Cham, 2020) pp. 439-484. [8] P. Zyla et al. (Particle Data Group), PTEP 2020, 083C01 (2020). [9] E. Gatti, A. Geraci, and G. Ripamonti, Nuclear Instruments and Methods in Physics Research Section A: Accelerators, Spectrometers, Detectors and Associated Equipment 381, 117 (1996). [10] A. Regadío, J. Tabero, and S. Sánchez-Prieto, Nuclear Instruments and Methods in Physics Research Section A: Accelerators, Spectrometers, Detectors and Associated Equipment 811, 25 (2016). [11] H. Spieler, Nuclear Instruments and Methods in Physics

Research Section A: Accelerators, Spectrometers, Detectors and Associated Equipment 636, S149 (2011), 7th International “Hi-roshima” Symposium on the Development and Application of Semiconductor Tracking Detectors. [12] V. Radeka, *IEEE Transactions on Nuclear Science* 15, 455 (1968). [13] E. Gatti and P. F. Manfredi, *La Rivista del Nuovo Cimento* (1978-1999) 9, 1 (1986). [14] G. Gerardi and L. Abbene, *Nuclear Instruments and Methods in Physics Research Section A: Accelerators, Spectrometers, Detectors and Associated Equipment* 768, 46 (2014). [15] Q. Wang, H. Huang, X. Ma, Z. Shen, C. Zhong, W. Ding, W. Zhou, and J. Zhou, *Applied Radiation and Isotopes* 190, 110515 (2022). [16] A. Regadío, S. Sánchez-Prieto, J. Tabero, and D. M. González-Castaño, *Nuclear Instruments and Methods in Physics Research Section A: Accelerators, Spectrometers, Detectors and Associated Equipment* 795, 115 (2015). [17] Glenn G. Knoll, John Wiley & Sons, Inc. (John Wiley & Sons, 2010). [18] B. Loo, F. Goulding, and D. Gao, *IEEE Transactions on Nuclear Science* 35, 114 (1988). [19] C. Imperiale and A. Imperiale, *Measurement* 30, 49 (2001). [20] M. Wang, J. Zhou, X. Wang, H. Wang, Y. Liu, X. Hong, and T. Yang, *Applied Radiation and Isotopes* 196, 110772 (2023). [21] V. T. Jordanov, *Nuclear Instruments and Methods in Physics Research Section A: Accelerators, Spectrometers, Detectors and Associated Equipment* 805, 63 (2016), special Issue in memory of Glenn F. Knoll. [22] X.-Y. Wang et al., *Nuclear Science and Techniques* 33, 46 (2022). [23] V. T. Jordanov and K. V. Jordanova, *Nuclear Instruments and Methods in Physics Research Section A: Accelerators, Spectrometers, Detectors and Associated Equipment* 1044, 167421 (2022). [24] A. Regadío and S. Sánchez-Prieto, *Nuclear Instruments and Methods in Physics Research Section A: Accelerators, Spectrometers, Detectors and Associated Equipment* 888, 228 (2018). [25] Z. Deng, X. Zhao, H. Ding, Y. Deng, X. Cao, and K.-V. Yuen, in *2020 IEEE International Conference on Signal Processing, Communications and Computing (ICSPCC)* (2020) pp. 1-6. [26] M.-R. Mohammadian-Behbahani and S. Saramad, *Nuclear Instruments and Methods in Physics Research Section A: Accelerators, Spectrometers, Detectors and Associated Equipment* 897, 1 (2018). [27] S. Miłosz, K. Tudyka, A. Walencik-Łata, S. Barwinek, A. Bluszcz, and G. Adamiec, *IEEE Transactions on Nuclear Science* 64, 2536 (2017). [28] M. Bolic, V. Drndarevic, and W. Gueaieb, *IEEE Transactions on Instrumentation and Measurement* 59, 122 (2010). [29] H.-Q. Huang, X.-F. Yang, W.-C. Ding, and F. Fang, *Nuclear Science and Techniques* 28, 12 (2017). [30] B. Jeon, S. Lim, E. Lee, Y.-S. Hwang, K.-J. Chung, M. Moon, *IEEE Transactions on Nuclear Science* 69, 1344 (2022). [31] A. Regadío, L. Esteban, and S. Sánchez-Prieto, *Nuclear Instruments and Methods in Physics Research Section A: Accelerators, Spectrometers, Detectors and Associated Equipment* 1005, 165403 (2021). [32] H. Sakai, A. Uritani, Y. Takenaka, C. Mori, and T. Iguchi, *Nuclear Instruments and Methods in Physics Research Section A: Accelerators, Spectrometers, Detectors and Associated Equipment* 421, 316 (1999). [33] V. T. Jordanov and D. L. Hall, in *2002 IEEE Nuclear Science Symposium Conference Record*, Vol. 1 (IEEE, 2002) pp. 140- [34] C. R. Harris et al., *Nature* 585, 357 (2020). [35] M. Abadi et al., “TensorFlow: Large-scale

machine learning on heterogeneous systems,” (2015), software available from tensorflow.org. [36] L. Tang, K. Shi, H. Shen, and Y. Soh, IEEE Transactions on Nuclear Science 70, 2479 (2023). [37] S. Ayuso, J. I. García Tejedor, J. J. Blanco, R. Gómez Herrero, O. García Población, J. Medina, M. Prieto, A. López Comazzi, in 36th International Cosmic Ray Conference (ICRC2019), International Cosmic Ray Conference, Vol. 36 (2019) p. 180. [38] M. K. Dağ, T. Güver, G. Gürkan, E. Aktaş, S. Özkorucuklu, S. Ayuso, J. J. Blanco, Z. F. Bostanci, B. Begiçarslan, M. T.

Sağlam, A. Polatoğlu, and C. Yeşilyaprak, Advances in Space Research 76, 1906 (2025). [39] A. Regadío, J. I. García Tejedor, S. Ayuso, Óscar García Población, J. J. Blanco, S. Sánchez-Prieto, and Óscar Rodríguez Polo, Nuclear Instruments and Methods in Physics Research Section A: Accelerators, Spectrometers, Detectors and Associated Equipment 973, 164166 (2020). [40] A. Regadío, J. J. Blanco, J. I. García Tejedor, S. Ayuso, I. Vrublevskyy, and S. Sánchez-Prieto, Advances in Space Research 72, 3428 (2023). [41] H.-Y. Shen, J.-L. Zhang, J. Zhang, and J.-H. Zhou, Nuclear Science and Techniques 35, 136 (2024).

Note: Figure translations are in progress. See original paper for figures.

Source: ChinaXiv – Machine translation. Verify with original.